ADVANCED FUNCTIONAL MATERIALS
www.afm-journal.de

Combining Janus Separator and Organic Cathode for Dendrite-Free and High-Performance Na-Organic Batteries

Yan Wu, Xingchao Wang, Fei Zhang, Lijuan Hai, QiHua Chen, Cuiqin Chao, Aikai Yang, Ying Sun,* and Dianzeng Jia**

The growth of Na-dendrites and the dissolution of organic cathodes are two major challenges that hinder the development of sodium-organic batteries (SOBs). Herein, a multifunctional Janus separator (h-BN@PP@C) by using an interfacial engineering strategy, is proposed to tackle the issues of SOBs. The carbon layer facing the organic cathode serves as a barrier to capture dissolved organic materials and enhance their utilization. Meanwhile, the h-BN layer facing the Na anode possesses high thermal conductivity and mechanical strength, which mitigates the occurrence of localized-temperature "hot spots" and promotes the formation of a NaF-enriched SEI, thereby suppressing dendrite growth. Consequently, the Janus separator enables a stable Na plating/stripping cycling for 1000 h at 3 mA cm^{-2}. Equipped with the Janus separator, organic cathodes including dibenzo[b,i] thianthrene-5,7,12,14-tetraone (DTT), pentacene-5,7,12,14-tetrone and Calix[4]quinone cathodes demonstrate high capacity and remarkable cycling performance. In particular, the DTT exhibits a bipolar co-reaction storage mechanism and achieves an ultrahigh capacity (≈342.6 mAh g^{-1}), long-term cycling stability (capacity decay rate of 0.15% per cycle over 550 cycles at 500 mA g^{-1}) and fast kinetics (1000 mA g^{-1}≈2.8 C). This study offers a straightforward, effective, and promising solution to address the challenges in SOBs.

1. Introduction

The insufficient reserves and uneven distribution of lithium have become key constraints to the development of energy storage systems.[1] As an alternative, abundant sodium resources and organic materials with flexible molecular structures make SOBs have great application potential.[2–5] Despite the great progress in research, the practical process of SOBs still faces some scientific challenges. For the cathode, organic electrodes and their discharge products can be dissolved in an organic electrolyte and diffuse unimpeded through the separator to the anode due to the concentration gradient effect. Even worse, the dissolved materials may react directly with the anode or electrodeposition on the surface until they are depleted.[6,7] As a consequence, the undesirable phenomena ultimately lead to severe self-discharge, capacity decay, undesirable cycling stability, and corrosion of the Na anodes. In terms of anode, Na anode suffers from an unstable SEI and growth of dendrites. These adverse effects can lead to continuous electrolyte consumption, increased polarization, and potentially thermal runaway by shorting failure.[8–11]

To date, several strategies have been proposed to address the aforementioned issue facing the organic cathode (e.g., molecular structure design[12–14] and electrolyte modulation[15–17]) and the Na anode (e.g., artificial SEI[18–20] and hosts[21–23]). However, these strategies primarily focus on addressing the existing shuttle effect of organic electrodes or the challenges of Na anode dendrite growth and fail to achieve simultaneous enhancements in cathodic and anodic performance.

Separators in battery system is an important component, in addition to the important role of separating cathode from anode,[24]

Y. Wu, X. Wang, F. Zhang, L. Hai, Q. Chen, C. Chao, D. Jia
State Key Laboratory of Chemistry and Utilization of Carbon Based Energy Resources
Key Laboratory of Advanced Functional Materials
Autonomous Region
Institute of Applied Chemistry
College of Chemistry
Xinjiang University
Urumqi, Xinjiang 830046, P. R. China
E-mail: xcwang@xju.edu.cn; jdz@xju.edu.cn

A. Yang
Institute of Energy and Climate Research
Materials Synthesis and Processing (IEK-1)
Forschungszentrum Jülich GmbH
52425 Jülich, Germany

Y. Sun
Xinjiang Uygur Autonomous Region Product Quality Supervision and Inspection Institute
Key Laboratory of Improvised Explosive Chemicals for State Market Regulation
Urumqi, Xinjiang 830011, P. R. China
E-mail: ichemabc@126.com

The ORCID identification number(s) for the author(s) of this article can be found under https://doi.org/10.1002/adfm.202309552

DOI: 10.1002/adfm.202309552

but also as a channel for the transmission of ions.[25,26] In recent reports, a few strategies for functionalized separators have achieved some achievement in solving the issues of organic cathode or Na anode.[27–30] The crucial challenge in designing functional separators for SOBs is to effectively inhibit shuttling and reduce irreversible losses of electroactive material while preventing corrosion of Na anodes, controlling dendritic growth, and inducing the formation of uniform SEI layers.

Herein, we present a Janus separator constructed using h-BN and carbon on PP to simultaneously solve the organic cathodic dissolution and Na anodic dendrites that plague SOBs. The high thermal conductivity of h-BN (≈400 W m^{-1} K^{-1}) enables efficient heat dissipation during the cycling process, effectively preventing the growth of Na-dendrite. Additionally, it exhibits reliable mechanical strength (220–510 N m^{-1}),[31–34] and promotes the formation of a uniform NaF-enriched SEI on the anode surface.[35,36] Moreover, the h-BN layer effectively blocks the pores of the separator, inhibiting the movement of dissolved organic cathode. The carbon coating towards the organic cathode acts as a physical barrier layer to trap and anchor the dissolved organic material, thus preventing shuttling and ultimately improving the utilization of the electroactive material.[28,37] Hence, the Janus separators enhance the open circuit voltage (OCV) stability, rate performance and cycling performance of the Na//DTT cells. In addition, organic materials including PT and C4Q also exhibit higher specific capacity and stable cycling. The simple preparation of multifunctional Janus separators solves the inherent problems and provides new ideas for the design of high-performance SOBs.

2. Results and Discussion

2.1. Characteristics of Janus Separator

The h-BN@PP@C separator with dual coating layers was prepared by a cost-effective and mass-producible doctor-blade technique. And the thickness of the coating can be easily controlled by adjusting the thickness of the blade. The cross-section image displays that the thicknesses of the h-BN layer and carbon layer are ≈17 and 5 µm, respectively (**Figure 1**a). In addition to thickness, weight is another important parameter to consider for the practical application of the separator. The weight of the h-BN@PP@C separator is ≈3.9 mg, higher than the weight of the PP separator (2.16 mg) under the same diameter (16 mm). This lightweight structure contributes to achieving high energy density. Furthermore, as shown in Figure S1 (Supporting Information), the h-BN@PP@C separator exhibits great mechanical stability and is capable of withstanding folding due to the strong adhesion between the separator and both powders (carbon and h-BN).

As shown in Figure 1b, the commercial PP separator exhibits a significant number of pores, ranging in diameter from several nanometers to several hundred nanometers. These pores allow for unrestricted diffusion of dissolved organic material to the anode, resulting in the occurrence of the shuttle effect. However, upon applying the coating, the large pores of the PP separator are effectively covered by h-BN and carbon layers, which are arranged in parallel and tightly packed on the surface, leaving no areas exposed (Figure 1c,d). The porous properties and pore size distribution of the h-BN@PP@C separator were studied by N_2 adsorption/desorption isotherms (Figure 1e,f). It can be observed that the curve is type-IV isotherm with a hysteresis between P/P_0 of 0.9–1.0, indicating the presence of a porous structure. The pore size is mainly in the range of 3–10 nm (the average pore size of commercial PP separators is 43 nm). The calculated BET surface area of the h-BN@PP@C separator was 29.03 m^2 g^{-1}, considerably smaller than those of the PP separator (78 m^2 g^{-1}).[37] Owing to the dense coating covering the large pores of the PP separator, the reduction in pore size and specific surface area makes it more difficult for dissolved organic materials to diffuse through a separator.

A separator with favorable wetting performance is beneficial for achieving fast kinetics and reducing the polarization of SOBs. Therefore, the wetting performance of the h-BN@PP@C separator was evaluated by electrolyte contact angle measurements (Figure 1g). Compared to the PP separator (26.2°), the contact angle is smaller on both the h-BN side (19.8°) and the carbon side (6.7°). The h-BN@PP@C separator with a smaller contact angle accelerates electrolyte penetration, reduces migration resistance at the electrode/electrolyte interface and facilitates Na^+ transport.[38] To further understand Na-ion transport behavior through the PP and h-BN@PP@C separator, the Na^+ conductivity (σ) was measured by electrochemical impedance spectroscopy (EIS) with assembled SS//SS cells (Figure 1h). The h-BN@PP@C separators show significantly lower bulk resistance compared with PP. The Na^+ conductivity of the h-BN@PP@C separators is 0.38 mS cm^{-1}, versus being 0.076 mS cm^{-1} for PP. The h-BN@PP@C separator with favorable wetting performance can facilitate the conduction of Na^+ thus obtaining higher ionic conductivity.

The thermal stability and thermal conductivity of separators are key parameters that prevent thermal runaway and dendrite growth, which can induce rapid Na-dendrite growth and short-circuiting.[39] A more uniform thermal distribution contributes to stable Na plating/stripping cycling. To investigate this, we conducted a comparison between the PP and h-BN@PP@C separators under a point heat source at 70 and 100 °C, respectively. An infrared thermal image was utilized to map the temperature distribution of the two separators (Figure 1i,j). The temperature spike in the PP separator is ≈69.9 °C at the hot spot, whereas the temperature spike in the h-BN@PP@C separator is reduced to 67.0 °C due to the enhanced heat spreading. When the hot spot temperature rose to 100 °C, the h-BN layer of the h-BN@PP@C separator shows a smaller temperature spike (92.4 °C) compared with PP (100.7 °C). These results demonstrate that the h-BN@PP@C separator with uniform heat distribution promotes homogeneous sodium deposition and improves cycling performance.

2.2. The Effect of Janus Separator on Na Anodes

The influence of a modified separator on block Na dendrite growth was investigated using a Na//Na symmetric cell. The cells were deposited at a current density of 3 mA cm^{-2} for 1 h (**Figure 2**a). The cells with the PP separators show a sudden drop in voltage after a few tens of hours and eventually fail after 100 h with a drastic change in potential. Such poor performance is attributed to the repeated formation/destruction of SEI and the growth of dendrites on the Na anode. The C@PP

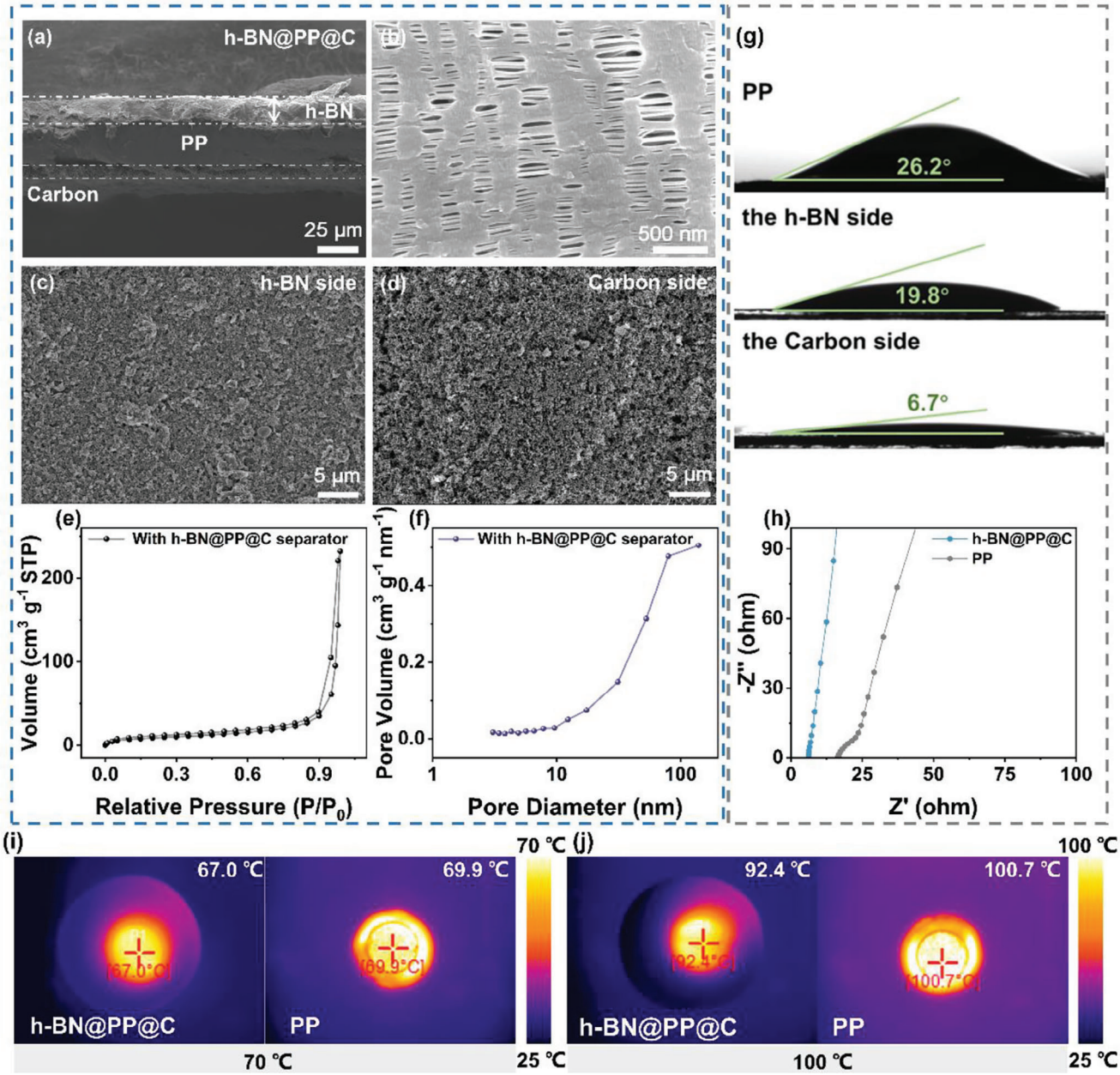

Figure 1. Characterization of separators. SEM images of a) Cross-section of the h-BN@PP@C separator, b) PP separator, c) h-BN layer, and d) carbon layer. e) N_2 sorption isotherm curves and f) Pore-size distribution of the h-BN@PP@C separator. g) Contact angle of electrolyte on the PP and h-BN@PP@C separators. h) EIS Nyquist plots of the SS//SS cells with different separators. Infrared thermal imaging of the PP and h-BN@PP@C separators at i) 70 °C and j) 100 °C, respectively.

separator exhibits a stable overpotential (≈31 mV) and experiences a short circuit after 300 h. In contrast, the h-BN@PP separator shows good cycle stability with a low overpotential of 16 mV over 700 h. Notably, the h-BN@PP@C symmetric cell displays a stable voltage profile and a small overpotential (≈14 mV) over 1000 h. This result demonstrates the superiority of the Janus separator in terms of improved interfacial stability and circulation.

To intuitively demonstrate the superiority of the Janus separator, the fast plating/stripping behavior of Na^+ in the h-BN@PP@C cells was further evaluated at various current densities ranging from 1 to 10 mA cm^{-2} (Figure 2b–f). The overpotential of the h-BN@PP@C symmetrical cell increases with the increase of current density but remains stable without obvious fluctuations. Even at a high current density of 10 mA cm^{-2}, the h-BN@PP@C symmetrical cells show a low overpotential (≈80 mV). When the current density is adjusted back to 1 mA cm^{-2}, the cells continue to cycle stably in the subsequent cycles. This result demonstrates that the h-BN@PP@C separator satisfies the requirement for high charge/discharge rates in

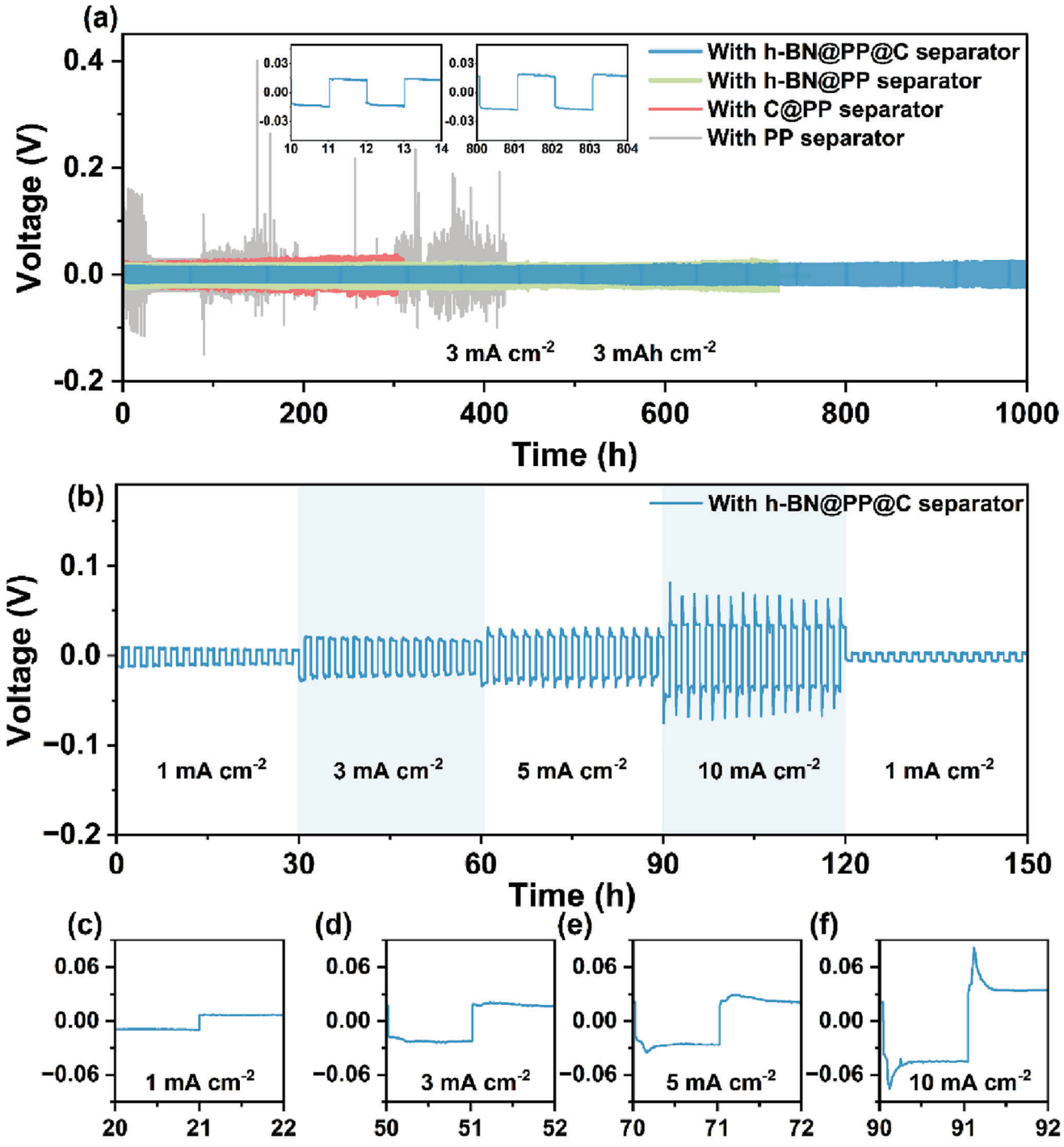

Figure 2. a) Cyclability of the Na//Na symmetric cells with different separators at 3 mA cm^{-2}, 3 mAh cm^{-2}, respectively (Insert figure: enlarged view of the curves of the h-BN@PP@C symmetric cells). b) Rate performance of the Na//Na cells with h-BN@PP@C separator at various current densities and c–f) corresponding enlarged voltage plots of (b).

practical SOBs. These enhanced plating/stripping performances of the cycling and rate performance tests can be attributed to the effective solution of the intrinsic dendrite problem by the designed Janus separator. Furthermore, the h-BN@PP@C separator enables high coulombic efficiency of about 99.2% for Na//Cu asymmetric cells (Figure S2a,b, Supporting Information), demonstrating the superiority of the Janus separator in terms of improved interfacial stability and circulation.

To further investigate the effect of the Janus separator on Na dendrite growth, the Na anode in the Na//DTT cells with PP and h-BN@PP@C separator were disassembled after 100 cycles. The anode obtained from the PP cell becomes rough and porous

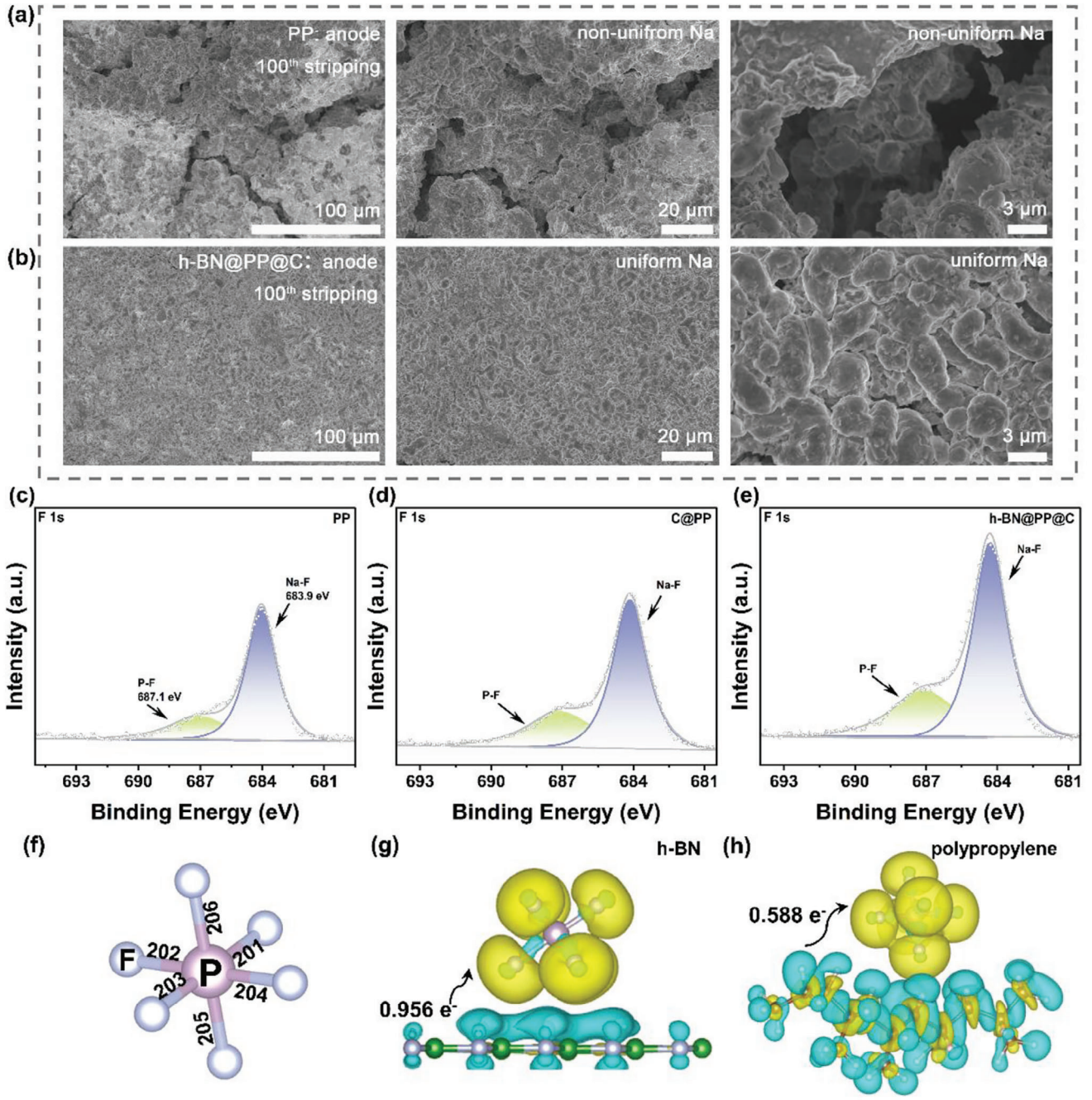

Figure 3. Top-down SEM images of the Na anodes in the Na//DTT cells with a) PP and b) h-BN@PP@C separators. The F 1s spectrum of the Na anode after 100 cycles at 200 mA g^{-1} with c) PP, d) C@PP and e) h-BN@PP@C separators. Changes in f) bond length, g) charge density of PF_6^- upon influences of h-BN@PP@C separator, and h) charge density of PF_6^- upon influences of PP separator.

with noticeable Na-dendrites (**Figure 3**a). This results in continuous electrolyte consumption and inferior cycle stability performance. In contrast, the Na anode in the h-BN@PP@C cell exhibits no Na-dendrites and cracks on the surface even after 100 cycles (Figure 3b). This result demonstrates that the Janus separator induces the uniform deposition of Na plating/stripping and successfully inhibits the dendrite growth. XPS analysis was performed to investigate the mechanism by which Janus isolates inhibit dendrites (Figure 3c–e). The F 1s spectrum shows a peak at 684.3 eV, indicating the presence of the Na—F bond of NaF, which is an important component of SEI. It is noteworthy that the peak intensity of the Na—F bond at the Na anode in the h-BN@PP@C cell is significantly higher compared to that in the PP and C@PP cells. This suggests that the h-BN coating induces the formation of a NaF-enriched SEI. The NaF-enriched SEI demonstrates both high diffusivity and strong adhesion to Na anodes, effectively

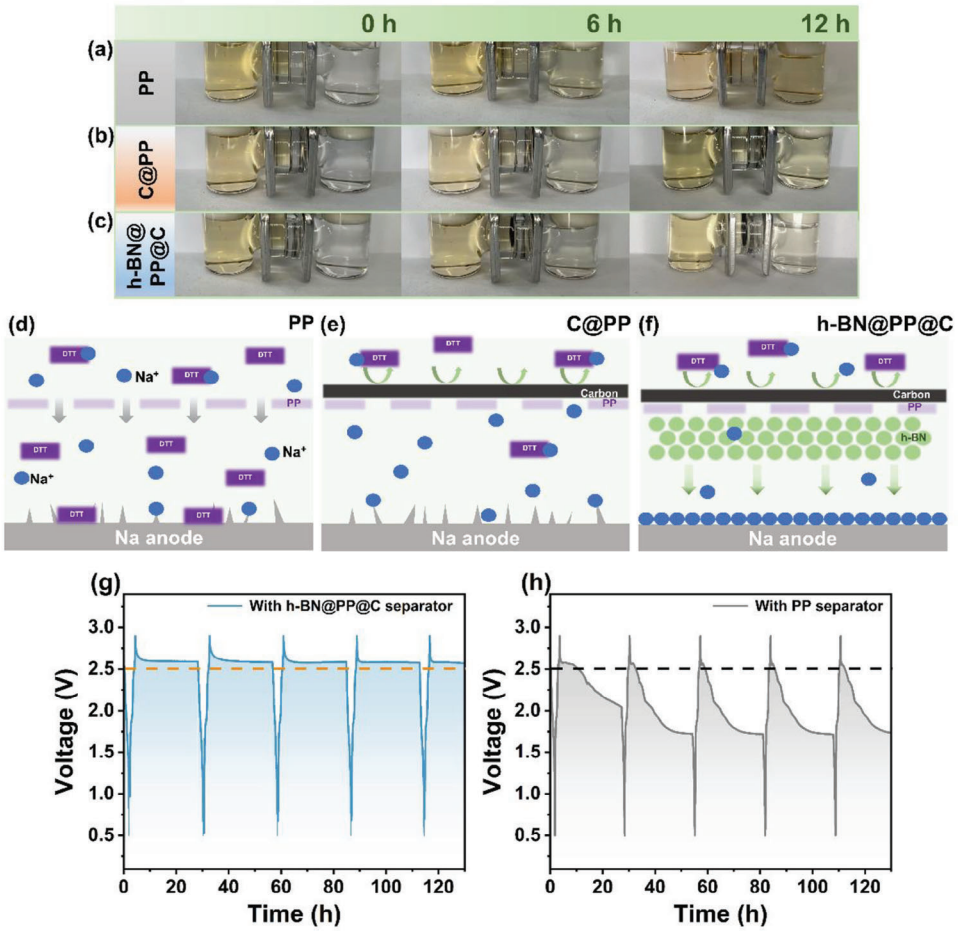

Figure 4. a–c) Visual shuttling contrast of DTT in DME with different separator. d–f) Schematic of diffusion of Na and organic molecules in different separators. Self-discharge characteristics of the Na//DTT cells with g) h-BN@PP@C and h) PP separators.

suppressing adverse reactions between electrodes and electrolytes, as well as dendrite growth.[34]

To further elucidate the correlation between NaF-enriched SEI formation and the Janus separator, density functional theory (DFT) calculations were conducted (Figure S3a,b, Supporting Information). Initially, the impact of h-BN on the P—F bond of $NaPF_6$ was simulated. The result reveals that the bond length of the P—F bond in the h-BN@PP@C cell is significantly longer than that in the PP cell, indicating that the former is more prone to decomposition and SEI formation (Figure 3f; Table S1, Supporting Information).[40] Furthermore, Bader charge analysis was employed to evaluate the charge transfer between P adatoms of PF_6^- and the separators. As deposited in Figure 3g,h, the charge transfer is −0.956 |e| for the h-BN@PP@C separator, which is smaller than that on the PP separator (−0.588 |e|) (Table S2, Supporting Information). This suggests that the introduction of h-BN leads to more electron transfer, ultimately destabilizes the structure of PF_6^- and leads to the formation of a NaF-enriched SEI. Based on this result, the mechanism of the Janus separator to induce inorganic SEI formation can be inferred, the structure of $NaPF_6$ becomes more unstable under the influence of the h-BN coating layer, and the free F atoms can form more of the NaF-enriched SEI.

2.3. The Effect of Janus Separator on DTT Cathodes

H-type cells were utilized to investigate the shuttle inhibition effect of the Janus separator on the DTT cathode (**Figure 4**a–c). The concentration gradient effect exists as the dissolved material diffused through a separator to the other side. The PP separator has a greater porosity, which allows DTT molecules to diffuse into the right chamber, resulting in a color change from colorless to yellow. In contrast, the C@PP separator exhibits hysteresis of DTT shuttling, indicating its efficient rescue of trapped active materials. Moreover, the h-BN@PP@C separator with a smaller porosity, effectively inhibits the diffusion of DTT even after 12 h, indicating that the dual coating layers provide an excellent blocking effect as a barrier by creating a physical barrier to achieve the inhibition of the "shuttle effect".[41,42] This finding provides strong evidence for the remarkable shuttle effects that are suppressed by the h-BN@PP@C separator, which can be clearly illustrated by the schematic. Commercial PP separators have inert Na^+ conductivity, with the ions concentrated around the pores, resulting in an uneven distribution of Na^+. Unstable sodium deposition increases the risk of dendritic growth, which eventually leads to the formation of "dead Na". Meanwhile, the PP separator is unable to suppress the DTT molecules shuttle (Figure 4d). In contrast,

the C@PP separators can effectively capture dissolved cathode materials and also provide a barrier to achieve the inhibition of the "shuttle effect". Despite some improvements in the C@PP cell, the anode is still corroded due to insufficient interception of dissolved organic molecules (Figure 4e). In the h-BN@PP@C cells, the h-BN layer has sufficient mechanical strength to prevent the formation of dendrites while inducing the formation of the NaF-enriched SEI. Therefore, by combining the benefits of h-BN and carbon coating layers, the h-BN@PP@C separator demonstrates the ability to effectively address the challenges posed by organic cathodes and Na anodes simultaneously (Figure 4f). This allows for the achievement of high performance in SOBs.

To further evaluate the effectiveness of the Janus separator in suppressing shuttle effects, a self-discharge test was conducted, since the self-discharge behavior is caused by the reaction of dissolved organic material with the Na anode. The Na//DTT cells with different separators were tested at 150 mA g^{-1} (Figure 4g,h). The cells were rested for 24 h after each cycle and the change in voltage over time was recorded. The OCV of the PP cell quickly falls to 1.7 V at rest, with a capacity loss of 40.3%. Conversely, the OCV of the h-BN@PP@C cell remains stable, always above 2.5 V with a slight loss of capacity.

In addition, galvanostatic intermittent titration technique (GITT) test was carried out to investigate the effect of Janus separator on the Na^+ diffusion coefficient ($D_{Na}{}^+$) (Figure S4a,b, Supporting Information). The calculated average $D_{Na}{}^+$ value for the h-BN@PP@C cells is$\approx 1 \times 10^{-13.71}$, which is higher than that of the PP cell ($\approx 1 \times 10^{-14.17}$), indicating faster Na^+ diffusion kinetics in the h-BN@PP@C cell. Such performance can be attributed to the carbon layer possessing high electrical conductivity and good interfacial compatibility, as the upper collector allows for the reutilization of trapped organic material and promotes rapid charging/discharging.

2.4. Electrochemical Performance of the Janus Cells

Given the resolution of the shuttle and dendrite growth problems using the Janus separator, comprehensive electrochemical tests on the assembled Na//DTT batteries were to evaluate its reliability in achieving high-performance SOBs. At the current density of 200 mA g^{-1}, the discharge/charge curves of Na//DTT batteries with the PP and h-BN@PP@C separators exhibit similar curves with the presence of multiple discharge plateaus (**Figure 5**a; Figure S5, Supporting Information). Note that the long voltage plateau during the first cycles can probably be attributed to the formation of CEI.[43–45] The capacity of the Na//DTT battery using the h-BN@PP@C separator is 342.6 mAh g^{-1} in the initial cycle and a stable capacity of 229.2 mAh g^{-1} can retain after 100 cycles (Figure 5b). In comparison, the discharge capacity of the Na//DTT batteries using the pp separator is merely 160.9 mAh g^{-1} after 100 cycles.

The rate performances of the Na//DTT cell with the Janus separator was also evaluated (Figure 5c). Compared to using the PP separator, the Na//DTT batteries using the h-BN@PP@C separator deliver high specific capacities of 349.5, 315.2, 299.1, and 286.5 mAh g^{-1} at 100, 200, 500, and 1000 mA g^{-1}, respectively. When the current density is adjusted to 100 mA g^{-1}, the battery maintains a high reversible capacity of 301.6 mAh g^{-1}. This superior rate performance can be attributed to the effective blocking of DTT molecules and the good interfacial compatibility of the h-BN@PP@C separator. The long-term cycling stability of the Na//DTT battery using h-BN@PP@C separator at high current densities was also explored (Figure 5d). After three activation cycles, the h-BN@PP@C cell exhibits a reversible capacity of 285.2 mAh g^{-1} at the current density of 500 mA g^{-1}. Even after 550 cycles, the capacity remains at 202.3 mAh g^{-1}, which is significantly higher compared to the capacities of the PP (90.6 mAh g^{-1}), C@PP (160.2 mAh g^{-1}) and the h-BN@PP batteries (132.4 mAh g^{-1}). These results confirm the effectiveness of the h-BN@PP@C separator in addressing the dissolution issue and improving the electrochemical stability of the resulting DTT. Furthermore, the h-BN@PP@C battery demonstrates excellent electrochemical even at a higher current density of 1000 mA g^{-1} ($\approx$2.8 C). A high reversible capacity of 215.4 mAh g^{-1} is obtained after 300 cycles, with a remarkable capacity retention of 70% (Figure 5e).

To assess the universality of the Janus separator in constructing high-performance and long-life SOBs, we designed and evaluated two additional batteries with PT (Figure 5f) and C4Q (Figure 5h) cathodes. Figure S6 (Supporting Information) shows the CV curve of the Na//PT battery with the h-BN@PP@C separator at a scan rate of 0.2 mV s^{-1}. Three reduction peaks are observed at 1.0, 1.6 and 2.2 V, corresponding to the reaction of the carbonyl group of PT with Na^+. Additionally, four oxidation peaks observed at 1.2, 1.7, 2.1, and 2.5 V represent the conversion of sodium enolates back to carbonyl groups (Figure S7a, Supporting Information). The Na//PT battery also exhibits an overlap charge and discharge curves with a specific capacity of 200.4 mAh g^{-1} even after 700 cycles at 500 mA g^{-1} (Figure 5g). This specific capacity significantly exceeds the discharge capacity of the PP battery, which is only 71.5 mAh g^{-1}. Moreover, the Na//C4Q battery using the h-BN@PP@C separator demonstrates improved cycling stability and capacity, maintaining a specific capacity of 213.3 mAh g^{-1} after 700 cycles compared to the PP battery (Figure 5i; Figure S7b, Supporting Information). These results highlight the beneficial role of the Janus separator in enhancing the electrochemical performance of both the Na//PT and Na//C4Q systems.

2.5. Reaction Mechanisms of DTT

To further investigate the overcapacity behavior of the DTT cathode, a series of research works was designed and conducted, including CV, ex situ IR, and ex situ XPS. Initially, the reduction/oxidation behavior of DTT was examined through CV testing (Figure S8, Supporting Information). It is worth noting that, besides the irreversible peak at 0.7 V in the first cycle, which could be attributed by CEI, five pairs of redox peaks appeared in subsequent cycles. These findings align with the discharge/charge curves and provide evidence for the multi-step electrochemical sodiation/desodiation process of the Na//DTT battery (**Figure 6**a). The ex situ FTIR spectra of DTT cathode were collected after the initial cycling at 200 mA g^{-1} (Figure S9, Supporting Information). The FTIR spectra show that the characteristic peaks of the C=O (1631 cm^{-1}) group gradually weaken

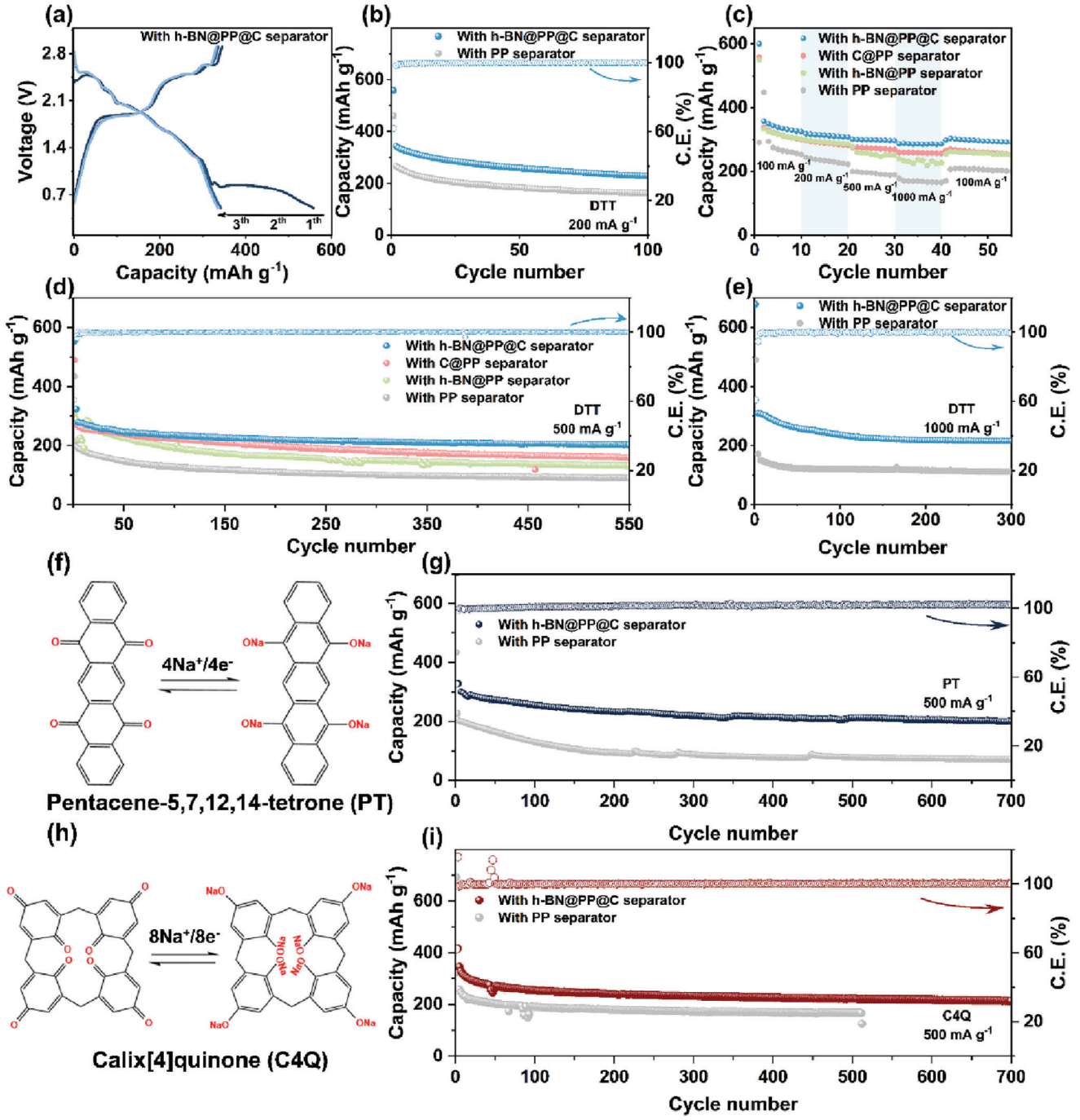

Figure 5. Electrochemical performance of batteries with different separators. a) Discharge/charge curves at 200 mA g^{-1}. b) Cycle performance and c) Rate performance of the Na//DTT batteries. Long-term cycling stability of the Na//DTT batteries at d) 500 mA g^{-1} and e) 1000 mA g^{-1}. f) Structures and energy storage mechanism of PT cathode. g) Cycle performance of the Na//PT batteries. h) Structures and energy storage mechanism of C4Q cathode. i) Cycle performance of the Na//C4Q batteries.

during the discharging (from point a to point b), indicating the coordination of Na^+ with the C=O group of DTT (Figure 6b). In the subsequent charging, the peak intensities gradually recover during the desodiation process (from point c to point d). The peak of PF_6^- located at 844.7 cm^{-1} is observed, which gradually strengthens as the Na//DTT cell charges to 2.6 V and reaches its maximum intensity at 2.9 V (Figure 6c), indicating the reversible insertion/extraction of PF_6^- in the DTT.

Figure S10 (Supporting Information) shows the full survey XPS spectrum of the DTT electrode at different states in the 2nd cycle. In the O 1s spectra (Figure 6d), the presence of the C=O peak gradually weakens during the discharged process (from

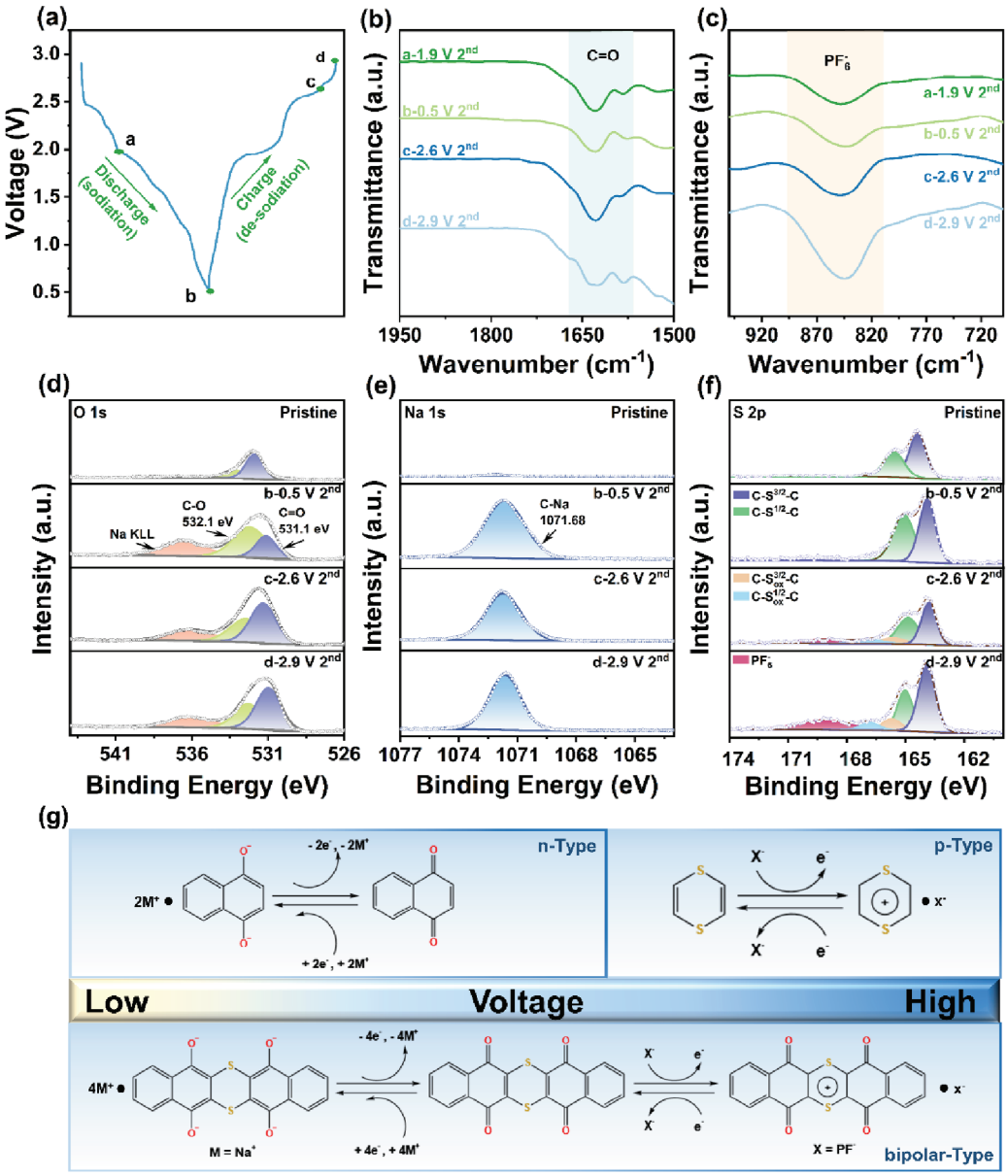

Figure 6. a) Discharge/charge curves of DTT cathode at the current density of 200 mA g^{-1}. Ex situ FTIR spectra of DTT cathode at different discharge/charge states: b) C=O bond, c) PF_6^-. Ex situ XPS spectra at different states: d) O 1s spectrum, e) Na 1s spectrum, f) S 2p spectrum. g) Structures and presumed energy storage mechanism of DTT cathode.

point b) and then strengthens during the charging process (from point b to point d). This observation is consistent with the FTIR analysis and confirms the reaction involving the C=O group. In the Na 1s spectra (Figure 6e), the strong relative peak intensity at the discharged state (point b) proves the insertion of Na^+, which decreases at the charged state (from point b to point d) due to Na extraction from DTT. In the S 2p spectra (Figure 6f), the peaks at 163.7 and 164.9 eV of pristine DTT cathode correspond to the neutral C-$S^{3/2}$-C and C-$S^{1/2}$-C groups, respectively. When charging to the 2.6 V state (point c), two new broad peaks are observed at 165.9 and 166.9 eV, which are attributed to the oxidized C-$S^{3/2}$-C and C-$S^{1/2}$-C groups, respectively. Upon charging to 2.9 V (point d), the intensities of the peaks are strengthened. Furthermore, a new peak at 168.8 eV is observed, which corresponds to the PF_6^- anion, providing additional evidence for the involvement of PF_6^- anion reaction.[46] These intriguing findings confirm the bipolar-type co-reaction mechanism of the DTT cathode and establish its potential as a promising new cathode for constructing high-performance SOBs (Figure 6g).

3. Conclusion

In summary, we have demonstrated an interface engineering strategy involving the use of a Janus separator to effectively inhibit both Na-dendrite growth and organic cathode dissolution simultaneously for SOBs. The h-BN coating, with its good wetta-

bility and thermal conductivity, promotes the formation of a NaF-enriched SEI, which enables a uniform Na-ion flux and prevents the generation of Na-dendrites. Additionally, the carbon coating functions as a conductive physical barrier, effectively increasing the utilization of the electroactive material and accelerating the kinetics, while also providing a barrier that enhances the long-cycle performance. Consequently, the Janus separator enables a dendrite-free long-lifespan of Na//Na cells over 1000 h with a stable overpotential of ≈14 mV. The Na//DTT battery with the Janus separator displays a high specific capacity of 285.2 mAh g^{-1} at 500 mA g^{-1} and great cycling performance over 550 cycles. Moreover, two other organic materials (PT and C4Q) using the Janus separator also exhibit enhanced capacities and cycling stability.

Supporting Information

Supporting Information is available from the Wiley Online Library or from the author.

Acknowledgements

This work was financially supported by the National Natural Science Foundation of China (21905242, 22065033, 21972123, and U2003307), the Nature Science Foundation of Xinjiang Province (2022B01024, 2022D01E35, and 2022D01A105).

Conflict of Interest

The authors declare no conflict of interest.

Data Availability Statement

The data that support the findings of this study are available from the corresponding author upon reasonable request.

Keywords

functional separator, Na dendrite, shuttle effect, sodium-organic batteries

Received: August 12, 2023
Revised: October 20, 2023
Published online:

[1] P. K. Nayak, L. Yang, W. Brehm, P. Adelhelm, *Angew.Chem., Int. Ed.* **2018**, *57*, 102.
[2] Z. Shadike, H. Lee, O. Borodin, X. Cao, X. Fan, X. Wang, R. Lin, S.-M. Bak, S. Ghose, K. Xu, C. Wang, J. Liu, J. Xiao, X.-Q. Yang, E. Hu, *Nat. Nanotechnol.* **2021**, *16*, 549.
[3] Z. Shadike, Y.-N. Zhou, L.-L. Chen, Q. Wu, J.-L. Yue, N. Zhang, X.-Q. Yang, L. Gu, X.-S. Liu, S.-Q. Shi, Z.-W. Fu, *Nat. commun.* **2017**, *8*, 556.
[4] Z. Shadike, H.-S. Lee, C. Tian, K. Sun, L. Song, E. Hu, I. Waluyo, A. Hunt, S. Ghose, Y. Hu, J. Zhou, J. Wang, P. Northrup, S.-M. Bak, X.-Q. Yang, *Adv. Energy. Mater.* **2019**, *9*, 1900705.
[5] E. Gabriel, C. Ma, K. Graff, A. Conrado, D. Hou, H. Xiong, *eScience* **2023**, *3*, 100139.
[6] Y. Lu, J. Chen, *Nat. Rev. Chem.* **2020**, *4*, 127.
[7] H. Zhang, Y. Gao, X.-H. Liu, Z. Yang, X.-X. He, L. Li, Y. Qiao, W.-H. Chen, R.-H. Zeng, Y. Wang, S.-L. Chou, *Adv. Funct. Mater.* **2021**, *32*, 2107718.
[8] Y. Zhao, Y. Ye, F. Wu, Y. Li, L. Li, R. Chen, *Adv. Mater.* **2019**, *31*, 1806532.
[9] C. Yan, X.-Q. Zhang, J.-Q. Huang, Q. Liu, Q. Zhang, *Trends Chem.* **2019**, *1*, 693.
[10] D. Lin, Y. Liu, Y. Cui, *Nat. Nanotechnol.* **2017**, *12*, 194.
[11] S. Ye, L. Wang, F. Liu, P. Shi, Y. Yu, *eScience* **2021**, *1*, 75.
[12] C. Luo, Y. Zhu, Y. Xu, Y. Liu, T. Gao, J. Wang, C. Wang, *J. Power Sources* **2014**, *250*, 372.
[13] Z. Song, T. Xu, M. L. Gordin, Y.-B. Jiang, I.-T. Bae, Q. Xiao, H. Zhan, J. Liu, D. Wang, *Nano Lett.* **2012**, *12*, 2205.
[14] Z. Song, Y. Qian, T. Zhang, M. Otani, H. Zhou, *Adv. Sci.* **2015**, *2*, 1500124.
[15] W. Zhang, H. Sun, Z. Sun, S. Liu, W. Huang, *Inorg. Chem. Front.* **2021**, *8*, 4751.
[16] W. Huang, Z. Zhu, L. Wang, S. Wang, H. Li, Z. Tao, J. Shi, L. Guan, J. Chen, *Angew.Chem., Int. Ed.* **2013**, *52*, 9162.
[17] Y. Hanyu, Y. Ganbe, I. Honma, *J. Power Sources* **2013**, *221*, 186.
[18] F. Liu, L. Wang, Z. Zhang, P. Shi, Y. Feng, Y. Yao, S. Ye, H. Wang, X. Wu, Y. Yu, *Adv. Funct. Mater.* **2020**, *30*, 2001607.
[19] W. Guo, W. Zhang, Y. Si, D. Wang, Y. Fu, A. Manthiram, *Nat. Commun.* **2021**, *12*, 3031.
[20] Q. Li, F.-L. Zeng, Y.-P. Guan, Z.-Q. Jin, Y.-Q. Huang, M. Yao, W.-K. Wang, A.-B. Wang, *Energy Storage Mater.* **2018**, *13*, 151.
[21] J. He, A. Manthiram, *Adv. Energy Mater.* **2020**, *10*, 2002654.
[22] M. Zhang, Y. Guo, Y. Wei, B. Wang, Y. Zhang, H. Wu, X. Zhou, Y. Zhang, Q. Wang, *J. Mater. Chem. A.* **2020**, *8*, 18987.
[23] S. Liu, J. Li, X. Yan, Q. Su, Y. Lu, J. Qiu, Z. Wang, X. Lin, J. Huang, R. Liu, B. Zheng, L. Chen, R. Fu, D. Wu, *Adv. Mater.* **2018**, *30*, 1706895.
[24] X. Huang, R. He, M. Li, M. O. L. Chee, P. Dong, J. Lu, *Mater. Today* **2020**, *41*, 143.
[25] P. Zhai, K. Liu, Z. Wang, L. Shi, S. Yuan, *J. Power Sources* **2021**, *499*, 229973.
[26] S. S. Zhang, *J. Power Sources* **2007**, *164*, 351.
[27] Y. Wang, C. Fang, Y. Huang, Q. Liu, R. Zhao, X. Ding, Y. Huang, *RSC Adv.* **2018**, *8*, 24900.
[28] Y. Pan, J. Hao, X. Zhu, Y. Zhou, S.-L. Chou, *Inorg. Chem. Front.* **2018**, *5*, 1869.
[29] J. Qin, H. Shi, K. Huang, P. Lu, P. Wen, F. Xing, B. Yang, M. Ye, Y. Yu, Z.-S. Wu, *Nat. Commun.* **2021**, *12*, 5786.
[30] X. Li, J. Zhang, X. Guo, C. Peng, K. Song, Z. Zhang, L. Ding, C. Liu, W. Chen, S. Dou, *Adv. Mater.* **2023**, *35*, 2203547.
[31] J. Wu, X. Li, Z. Rao, X. Xu, Z. Cheng, Y. Liao, L. Yuan, X. Xie, Z. Li, Y. Huang, *Nano Energy* **2020**, *72*, 104725.
[32] W. Luo, L. Zhou, K. Fu, Z. Yang, J. Wan, M. Manno, Y. Yao, H. Zhu, B. Yang, L. Hu, *Nano Lett.* **2015**, *15*, 6149.
[33] Md. M. Rahman, S. Mateti, Q. Cai, I. Sultana, Y. Fan, X. Wang, C. Hou, Y. Chen, *Energy Storage Mater.* **2019**, *19*, 352.
[34] J. Sheng, Q. Zhang, M. Liu, Z. Han, C. Li, C. Sun, B. Chen, X. Zhong, L. Qiu, G. Zhou, *Nano Lett.* **2021**, *21*, 8447.
[35] H.-J. Peng, D.-W. Wang, J.-Q. Huang, X.-B. Cheng, Z. Yuan, F. Wei, Q. Zhang, *Adv. Sci.* **2016**, *3*, 1500268.
[36] M. Ye, Y. Xiao, Z. Cheng, L. Cui, L. Jiang, L. Qu, *Nano Energy* **2018**, *49*, 403.
[37] Y. Sun, X. Wang, A. Yang, Y. Huang, W. Jia, D. Jia, F. Cheng, M. Xu, M. Li, Y. Lu, *Chem. Eng. J.* **2021**, *418*, 129404.
[38] Z. Luo, L. Liu, Q. Zhao, F. Li, J. Chen, *Angew. Chem., Int. Ed.* **2017**, *56*, 12561.
[39] Y. Zhu, J. Xie, A. Pei, B. Liu, Y. Wu, D. Lin, J. Li, H. Wang, H. Chen, J. Xu, A. Yang, C.-L. Wu, H. Wang, W. Chen, Y. Cui, *Nat. Commun.* **2019**, *10*, 2067.
[40] T. Kang, C. Sun, Y. Li, T. Song, Z. Guan, Z. Tong, J. Nan, C.-S. Lee, *Adv. Energy Mater.* **2023**, *13*, 2204083.

[41] M. Yao, S.-I. Yamazaki, H. Senoh, T. Sakai, T. Kiyobayashi, *Mater. Sci. Eng., B* **2012**, *177*, 483.
[42] T. B. Schon, B. T. Mcallister, P.-F. Li, D. S. Seferos, *Chem. Soc. Rev.* **2016**, *45*, 6345.
[43] T. Ma, Q. Zhao, J. Wang, Z. Pan, J. Chen, *Angew. Chem., Int. Ed.* **2016**, *55*, 6428.
[44] Y.-J. Mao, B.-X. Wang, Q.-Z. Wu, K. Zhou, S.-J. Lou, D.-Q. Xu, *Chem. Commun.* **2019**, *55*, 2019.
[45] M. R. Tuttle, S. Zhang, *Chem. Mater.* **2019**, *32*, 255.
[46] H. Cui, T. Wang, Z. Huang, G. Liang, Z. Chen, A. Chen, D. Wang, Q. Yang, H. Hong, J. Fan, C. Zhi, *Angew. Chem., Int. Ed.* **2022**, *61*, e202203453.